Structural refinement, optical and electrical properties of $[Ba_{1-x}Sm_{2x/3}](Zr_{0.05}Ti_{0.95})O_3$ ceramics

T. Badapanda · S. Sarangi · B. Behera ·
S. Anwar · T. P. Sinha · R. Ranjan ·
G. E. Luz Jr. · E. Longo · L. S. Cavalcante

Abstract Samarium doped barium zirconate titanate ceramics with general formula $[Ba_{1-x}Sm_{2x/3}](Zr_{0.05}Ti_{0.95})O_3$ [$x = 0$, 0.01, 0.02, and 0.03] were prepared by high energy ball milling method. X-ray diffraction patterns and micro-Raman spectroscopy confirmed that these ceramics have a single phase with a tetragonal structure. Rietveld refinement data were employed to model $[BaO_{12}]$, $[SmO_{12}]$, $[ZrO_6]$, and $[TiO_6]$ clusters in the lattice. Scanning electron microscopy shows a reduction in average grain size with the increase of Sm^{3+} ions into lattice. Temperature-dependent dielectric studies indicate a ferroelectric phase transition and the transition temperature decreases with an increase in Sm^{3+} ion content. The nature of the transition was investigated by the Curie–Weiss law and it is observed that the diffusivity increases with Sm^{3+} ion content. The ferroelectric hysteresis loop illustrates that the remnant polarization and coercive field increase with an increase in Sm^{3+} ions content. Optical properties of the ceramics were studied using ultraviolet–visible diffuse reflectance spectroscopy.

T. Badapanda (✉)
Department of Physics, C.V. Raman College of Engineering, Bhubaneswar 752054, Odisha, India
e-mail: badapanda.tanmaya@gmail.com

S. Sarangi · B. Behera
School of Physics, Sambalpur University, Jyoti Vihar Sambalpur 768019, Odisha, India

S. Anwar
Colloids and Materials Chemistry, Institute of Minerals and Materials Technology, Bhubaneswar 751013, Odisha, India

T. P. Sinha
Department of Physics, Bose Institute, Kolkata 700009, India

R. Ranjan
Department of Materials Engineering, Indian Institute of Science, Bangalore 560012, India

G. E. Luz Jr. · L. S. Cavalcante (✉)
CCN-DQ-GERATEC, Universidade Estadual do Piauí, João Cabral, N. 2231, P.O. Box 381, CEP: 64002-150 Teresina, PI, Brazil
e-mail: laeciosc@bol.com.br; laeciosc@gmail.com

E. Longo
Universidade Estadual Paulista-CDMF, P.O. Box 355, CEP. 14801-907 Araraquara, SP, Brazil

1 Introduction

Lead-based piezoceramics have raised considerable environmental concerns, so there is a great demand of finding suitable lead free materials with similar behavior as that of the lead based materials. Among these lead free materials, barium zirconate titanate $Ba(Zr_xTi_{1-x})O_3$ in short (BZT) is one of the most studied functional materials due to its various potential applications such as piezoelectric transducers, dynamic random access memory, tunable microwave devices as well as for electrical energy storage units [1–7]. A suitable ionic substitution at different atomic sites of ABO_3-type materials has a drastic effect on physical properties. The selection of dopants or substitutions at different atomic sites is based on many factors, including: (1) charge neutrality; (2) tolerance factor $t = (r_A + r_o)/\sqrt{2}(r_B + r_o)$ where r_A and r_B are the radius of the A and B

site ions, and r_o is the ionic radius of oxygen; (3) ionic radius; and (4) solubility/miscibility [8]. Much research has been expended to improve dielectric properties by controlling grain growth and by designing the microstructural homogeneity. The substitution of both isovalent and aliovalent cations in the perovskite lattice are essential in these modification mechanisms [9, 10].

Recently, several researchers reported that the addition of rare earth ions improves dielectric properties of BZT ceramics [11–15] due to its low leakage current behavior and low electric field. Thus, interesting microstructural and dielectric response features have been observed; e.g., the phase transition temperature is drastically decreased by the addition of rare earth ions [11], and relaxor-type behavior is induced [13]. Compositional alterations to BZT ceramics with rare earth doping have been studied either by ''donor-doping'' with an anionic compensation mechanism that induces cationic vacancies and defects and alters the properties or by ''acceptor-doping'' to further improve material performance [16, 17]. Trivalent rare earth cations have been widely used in modifications of barium titanate ceramics due to their special electronic structures and moderate ionic radii which facilitate their incorporation into both A-sites and B-sites in the ABO_3 lattice [18–20]. Watanabe et al. [21] reported three stages of the substitution of rare earth elements in $BaTiO_3$. In the first stage, Ti^{4+} ions located on the B-site were replaced mainly by rare earth elements; in the second stage, Ba^{2+} ions on the A-site were also replaced mainly by rare earth elements. The third stage was over limit of substitution and a secondary phase appeared. Recent studies on rare earth doping in BZT ceramics have shown the effects on structural, dielectric, relaxor and electrical properties which find potential applications in various tunable microwave devices [22–29].

Therefore, in this paper, we report on the structure and microstructure as well as dielectric and optical properties of $[Ba_{1-x}Sm_{2x/3}](Zr_{0.05}Ti_{0.95})O_3$ with [$x = 0$, 0.01, 0.02, and 0.03] synthesized by the high energy ball milling method. These ceramics were structurally characterized by X-ray diffraction (XRD) patterns, Rietveld refinement and micro-Raman (M-Raman) spectroscopy. Dielectric properties were investigated by a dielectric constant, dielectric loss measurements as a function of temperature and hysteresis loop, and finally, optical properties were analyzed by ultraviolet–visible (UV–vis) diffuse reflectance spectroscopy.

2 Experimental details

2.1 Synthesis of $[Ba_{1-x}Sm_{2x/3}](Zr_{0.05}Ti_{0.95})O_3$ ceramics

$[Ba_{1-x}Sm_{2x/3}](Zr_{0.05}Ti_{0.95})O_3$ ceramics [$x = 0$, 0.01, 0.02, and 0.03] (BSZT) were prepared by a combination of a solid state reaction and the high energy ball milling technique. The ball-to-powder ratio (BPR) was maintained at 20:1 by weight. $BaCO_3$ (99.9 %), Sm_2O_3 (99.9 %), ZrO_2 (99.8 %) and TiO_2 (99.95 %) were used as starting materials, and a stoichiometric amount of these materials was weighed. For proper mixing, the weighed powders were mixed in tungsten carbide balls (10 mm diameter) with toluene as the milling media for 5 h at 300 rpm. Milled powders were heat treated at 1,100 °C for 4 h by using a programmable furnace.

2.2 Characterizations of $[Ba_{1-x}Sm_{2x/3}](Zr_{0.05}Ti_{0.95})O_3$ ceramics

Synthesized powders were structurally characterized by XRD using a Philips diffractometer Model PW-1830 with Cu-K$_\alpha$ ($\lambda = 1.5418$ Å) radiation in a wide range of 2θ ($20° \leq 2\theta \leq 80°$) at a scanning rate of $2° \text{ min}^{-1}$. To measure electrical properties of BSZT ceramics, the discs were pressed uniaxially at 200 MPa with 2 wt% polyvinyl alcohol added as a binder. Then these discs were sintered at 1,200 °C for 4 h. Silver contacts were deposited on opposite disc faces and heated at 700 °C for 15 min. The frequency (42 Hz–1 MHz) and temperature-dependent (170–500 K) dielectric measurements were carried out using a Hioki (Japan) LCR tester connected to a computer. The UV–vis spectrum was taken using a Shimadzu (UV-2600) spectrophotometer in diffuse reflection mode. For the piezoelectric measurement the samples were polled at an electric field 1.1 kV/mm for 30 min. The piezoelectric measurement was carried out by using a piezometer system (Piezotest; PM 300).

3 Result and discussion

3.1 XRD analyses

Figure 1a–d shows the XRD pattern of BSZT powders with different compositions: (a) $x = 0$; (b) $x = 0.01$; (c) $x = 0.02$ and (d) $x = 0.03$ heat-treated at 1,100 °C for 4 h. XRD patterns indicated that all BSZT ceramic compositions [$x = 0$, 0.01, 0.02, and 0.03] exhibit a tetragonal structure with a space group of (P4/*mmm*; No. 221. All diffraction peaks are in good agreement with the respective Inorganic Crystal Structure Database (ICSD) card No. 88534 [30]; no deleterious phases related to pyrochlore phase were detected. An increase in the Sm^{3+} ion content concentration produces a slight displacement of XRD peaks positions to higher values of 2θ and a decrease in $a = b$ lattice parameters and the unit cell volume. However, these BSZT ceramics do not undergo any kind of phase transition within the composition range studied which indicates that the lattice distortion increases with a raise in the Sm^{3+} ion content and that the doping Sm^{3+} ions occupy the A-site of the ABO_3 perovskite-
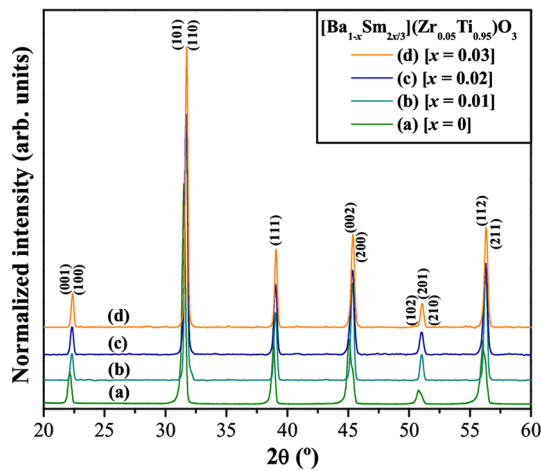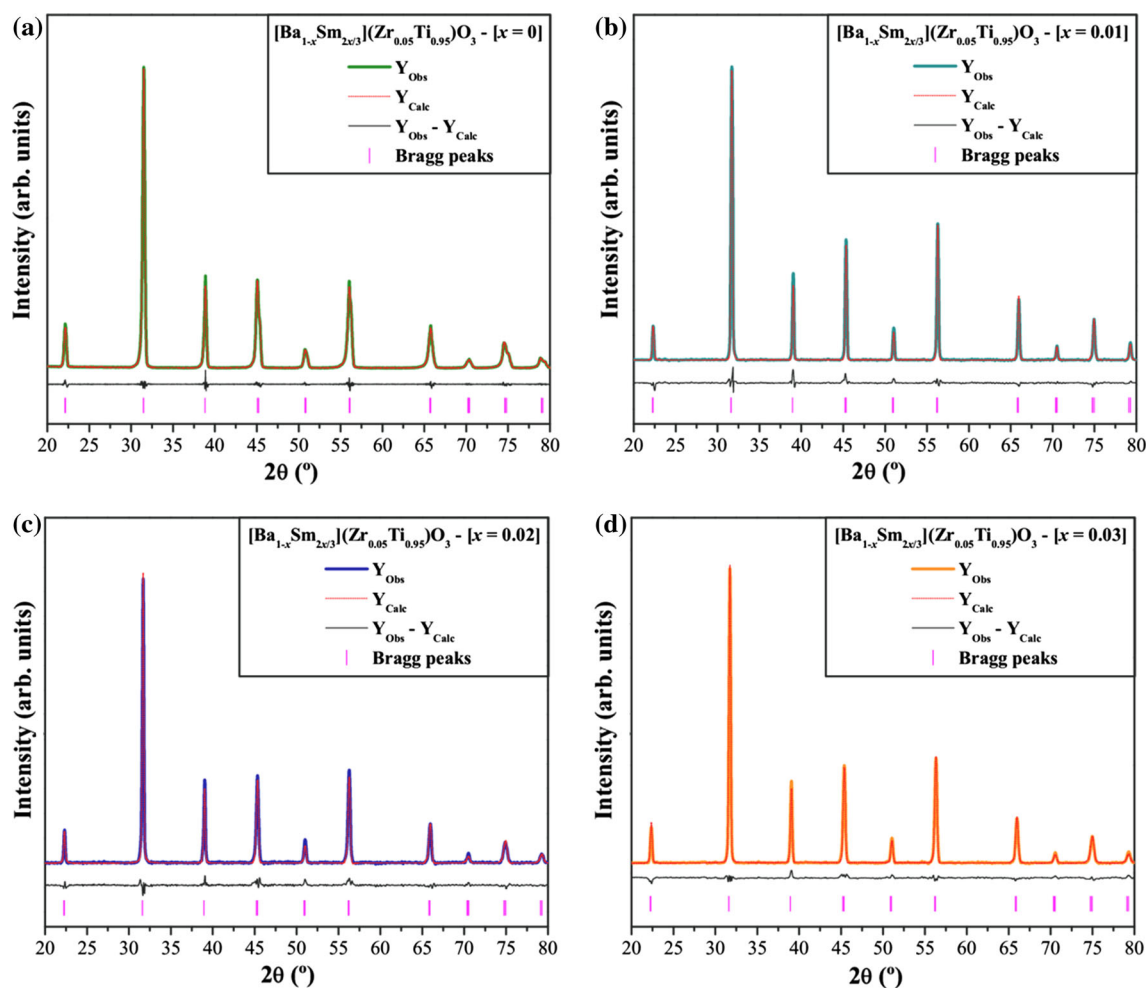
Fig. 1 XRD pattern of BSZT ceramic with different compositions: **a** $x = 0$; **b** $x = 0.01$; **c** $x = 0.02$, and **d** $x = 0.03$ heat-treated at 1,100 °C for 4 h

type tetragonal structure; this behavior can be related to the ionic radius of Sm^{3+} ions (0.109 nm) which is smaller than the ionic radius of Ba^{2+} ions (0.161 nm). According to Ostos et al. [24], the substitution of Ba^{2+} ions by Sm^{3+} ions in A-sites causes distortions in the BZT structure due to different ionic radii. Moreover, Fig. 1ES(a–d) illustrated a displacement of all of the diffraction peaks to high values of 2θ angles. According to Bragg's law [$\lambda.2d \sin \theta$], this displacement of 2θ angles occurs when there is a reduction in the unit-cell lattice parameters. Table 1 lists the results obtained by the analysis of the Rietveld refinement (Fig. 2a–d); the increase in the x content promotes a reduction in the lattice parameters of the $[Ba_{1-x}Sm_{2x/3}]$ $(Zr_{0.05}Ti_{0.95})O_3$ ceramic. This behavior is due to the replacement of [$3Ba^{2+}$ ions by $2Sm^{3+}$ ions with electronic balance], since Sm^{3+} ions have a minor electronic density in relation to Ba^{2+} ions.

Table 1 Lattice parameters, unit cell volume, c/a ratio, atomic positions and Rietveld refinement data for $[Ba_{1-x}Sm_{2x/3}](Zr_{0.05}Ti_{0.95})O_3$ ceramics with different compositions [(a) $x = 0$, (b) $x = 0.01$, (b) $x = 0.02$, and (b) $x = 0.03$]

Atoms	Wyckoff	Site	x	y	z	Occupancy
Ba	1a	4/mmm	0	0	0	1
Zr	1d	4/mmm	0.5	0.5	0.5	0.05
Ti	2h	4 mm	0.5	0.5	0.48324	0.95
O1	2h	4 mm	0.5	−0.02348	0.5	1
O2	4i	2 mm	0.5	0.47925	0	1

P4/mmm (123)—tetragonal ($a = b = 4.0244$ Å; $c = 4.0378$ Å; $c/a = 1.0033$; $V = 65.40$ Å^3) $R_p = 2.11$ %; $R_{exp} = 4.12$ %; $R_{wp} = 6.54$ %; $\chi^2 = 2.5186$ and GoF = 1.587

Atoms	Wyckoff	Site	x	y	z	Occupancy
Ba	1a	4/mmm	0	0	0	0.99
Sm	1a	4/mmm	0	0	0	0.01
Zr	1d	4/mmm	0.5	0.5	0.5	0.05
Ti	2h	4 mm	0.5	0.5	0.48734	0.95
O1	2h	4 mm	0.5	−0.02412	0.5	1
O2	4i	2 mm	0.5	0.463571	0	1

P4/mmm (123)—tetragonal ($a = b = 3.9852$ Å; $c = 4.0202$ Å; $c/a = 1.0088$; $V = 64.07$ Å^3) $R_p = 2.43$ %; $R_{exp} = 3.86$ %; $R_{wp} = 7.14$ %; $\chi^2 = 3.4225$ and GoF = 1.85

Atoms	Wyckoff	Site	x	y	z	Occupancy
Ba	1a	4/mmm	0	0	0	0.98
Sm	1a	4/mmm	0	0	0	0.02
Zr	1d	4/mmm	0.5	0.5	0.5	0.05
Ti	2h	4 mm	0.5	0.5	0.48235	0.95
O1	2h	4 mm	0.5	−0.02532	0.5	1
O2	4i	2 mm	0.5	0.44798	0	1

P4/mmm (123)—tetragonal ($a = b = 3.9814$ Å; $c = 4.03014$ Å; $c/a = 1.0122$; $V = 63.88$ Å^3) $R_p = 2.64$ %; $R_{exp} = 4.09$ %; $R_{wp} = 7.12$ %; $\chi^2 = 3.0276$ and GoF = 1.74

Atoms	Wyckoff	Site	x	y	z	Occupancy
Ba	1a	4/mmm	0	0	0	0.97
Sm	1a	4/mmm	0	0	0	0.03
Zr	1d	4/mmm	0.5	0.5	0.5	0.05
Ti	2h	4 mm	0.5	0.5	0.47681	0.95
O1	2h	4 mm	0.5	−0.02412	0.5	1
O2	4i	2 mm	0.5	0.44587	0	1

P4/mmm (123)—tetragonal ($a = b = 3.9689$ Å; $c = 4.02874$ Å; $c/a = 1.0151$; $V = 63.46$ Å^3) $R_p = 2.23$ %; $R_{exp} = 4.41$ %; $R_{wp} = 6.32$ %; $\chi^2 = 2.0535$ and GoF = 1.433

Fig. 2 Structural refinement using the Rietveld method of BSZT ceramic with different compositions: [**a** $x = 0$; **b** $x = 0.01$; **c** $x = 0.02$, and **d** $x = 0.03$] heat-treated at 1,100 °C for 4 h

3.2 Rietveld refinement data analyses

Figure 2a–d illustrate structural refinement using the Rietveld method and confirm that XRD patterns of BSZT ceramics with different compositions: [(a) $x = 0$; (b) $x = 0.01$; (c) $x = 0.02$, and (d) $x = 0.03$] heat-treated at 1,100 °C for 4 h are monophasic with a perovskite-type tetragonal structure.

Results obtained by using the Rietveld refinement method indicate good agreement between observed XRD patterns and fitted theoretical results. In the current study, we initially applied the Rietveld method or full pattern analysis for the structural refinement of BSZT ceramics. Observed experimental XRD pattern profiles of BSZT ceramics were refined with a theoretical line profile known as a Crystallographic Information File (CIF), which is related to the respective ICSD No. 88534 [30].

Rietveld refinements performed using the *ReX PD* program version 0.7.3 involved Rietveld texture and stress analysis. The optimized parameters were scale factor, background with exponential shift, exponential thermal shift, polynomial coefficients, basic phase, microstructure, crystal structure, structure factor extractor, shift lattice constants, profile half-width parameters (u, v, w), lattice parameters (a, b, c), Wyckoff, site occupancy, and occupancy. These parameters were used to obtain a structural refinement with better quality and reliability. All Rietveld refinements for BSZT ceramics were performed based on a perovskite-type tetragonal structure and a space group of *P4/mmm* (123) with better approximation and indexing with a CIF file as indicated in ICSD) card No. 88534 [30]. Recently Kalyani et al. [31] reported the coexistence of both orthorhombic and tetragonal phases at room temperature in $BaZr_xTi_{1-x}O_3$ ($0.02 \leq x \leq 0.07$), but we did not find any coexistence of phases in our study. According to Table 1, fitting parameters (R_p, R_{exp}, R_{wp}, χ^2, and GoF) indicate good agreement between refined and observed XRD patterns for all BSZT ceramics with a tetragonal

structure. This table also shows some variations in occupancy values due to the replacement of Ba atoms by Sm atoms which indicates that (Ba or Sm) atoms located in the same A-site occupy the same site in a fractional percentage. In addition, Fig. 2a–d confirm good agreement between observed XRD patterns and theoretical fit results and indicate the success of the Rietveld refinement method which displays small differences near zero in the intensity scale as illustrated by a line ($Y_{Obs} - Y_{Calc}$). The detailed fitting parameters and Wyckoff position obtained from Rietveld refinement are listed in Table 1.

In this table, the fit parameters (R_p, R_{exp}, R_{wp}, χ^2, and GoF) suggest that the refinement results are very reliable. Note that there are small variations in atomic positions related to the titanium and oxygen atoms while the barium, samarium, and zirconium atoms keep their fixed positions within the structure. These results confirm the existence of main distortions on octahedral [TiO$_6$] clusters in the tetragonal lattice of BSZT ceramics (Table 1).

3.3 Super cell representations with cluster modeling for [Ba$_{1-x}$Sm$_{2x/3}$](Zr$_{0.05}$Ti$_{0.95}$)O$_3$ ceramics

Figure 3a and b illustrate schematic representations of crystalline supercells for BSZT ceramics with (a) $x = 0$, and (b) $x \approx 0.02$.

Lattice parameters and atomic positions obtained from Rietveld refinements were used to model these supercells through the Diamond Crystal and Molecular Structure Visualization program (Version 3.2 g for Windows). Figure 3 illustrate supercells (1 × 5×4) for BSZT ceramics with (a) $x = 0$ and (b) $x \approx 0.02$ perovskite-type tetragonal structures, a space group of (P4/mmm) and a point-group symmetry (O$_h$). In these supercells, zirconium (Zr) and titanium (Ti) atoms are coordinated to six oxygen (O) atoms which form octahedral [TiO$_6$]/[ZrO$_6$] clusters [32]. Moreover, barium (Ba) atoms and samarium (Sm) atoms are coordinated to twelve O atoms which form cuboctahedral [BaO$_{12}$] clusters [33]. The cuboctahedron has twelve identical vertices which are formed by the meeting of two triangles and two squares, fourteen faces and twenty-four identical edges with each vertice separating a triangle from a square [34].

3.4 SEM images analyses

Figure 4a–d illustrate SEM images of sintered BSZT pellet sintered at 1,200 °C for 4 h, respectively.

The nature of BSZT ceramics microstructures indicates that the grains are densely packed. SEM images revealed large and small grains in microstructures for pure BZT ceramics and doped BSZT ceramics, respectively. Therefore, the incorporation of Sm^{3+} ions in the BZT lattice

A-site caused a reduction in average grain sizes. Sm^{3+} ions act as donors and retard the overall diffusion rate during the sintering process. The dissolution of Sm^{3+} ions as dopants in the perovskite lattice may increase oxygen vacancies and contribute to an increase in the overall cationic transport and thereby reduce the grain size [35]. Similar kind of decrement of grain size due to incorporation of rare earth is reported in literature [36, 37]. All compositions show non-uniformly distributed grains due to the characteristic matter transport mechanism between grains during the sintering process. At the initial stages of the solid state reaction, carbonates and oxides were ball milled in order to reduce the powder particle sizes. The heat promoted slow kinetics of inter- diffusion in contact points between particles with irregular morphologies. This diffusion resulted in irregularly shaped grains due to an elastic deformation caused by surface energy reduction in the contact interface by its orientation and mobility [38, 39].

### 3.5 Micro-Raman spectroscopy analyses

Figure 5a–d shows the M-Raman spectra of the [Ba$_{1-x}$Sm$_{2x/3}$](Zr$_{0.05}$Ti$_{0.95}$)O$_3$ ceramics with [$x = 0$, 0.01, 0.02, and 0.03), respectively.

Raman active modes of a tetragonal Ba(Zr$_{0.05}$Ti$_{0.95}$)O$_3$ ceramic powder in (P4mmm) symmetry induce the splitting of transverse and longitudinal phonons and result in split Raman active phonons as represented by Eq. (1) [40]:

$$3[A_1(TO) + A_1(LO)] + B_1 + 4[E(TO) + E(LO)] \qquad (1)$$

Modes split into longitudinal (LO) and transverse (TO) components which are associated with electrostatic forces and with lattice ionicity due to Ba^{2+} ions in the BZT lattice [41, 42]. The Raman spectrum in Fig. 5 shows phonon modes at 720 cm^{-1} (E(LO$_4$) + A1(LO$_3$)), 515 cm^{-1} (E(TO$_4$) + A1(TO$_3$)), 305 cm^{-1} ((E(TO$_3$) + E(LO$_2$) + B$_1$), 260 cm^{-1} (A$_1$(TO$_2$)) and 185 cm^{-1} (E(TO$_2$) + E(LO$_1$) + A$_1$TO$_1$) + A$_1$(LO$_1$)). E$_1$(TO$_1$) and E$_1$(TO$_2$) modes which are associated with the tetragonal phase transition are observed at 116 and 305 cm^{-1} whereas the A$_1$(LO$_3$) mode was found at 720 cm^{-1} with zirconium (Zr) substituting on titanium (Ti) sites; this feature of a BZT tetragonal arises for phonons propagating along the c-axis. No additional peak is observed with Sm^{3+} ion doping and confirms that there is no change in the structure which is in good agreement with XRD results. The A$_1$(TO) peak at 518 cm^{-1} and a band centered at 219 cm^{-1} are observed which may be due to intrinsic disorder in the phase [43]. The anti-resonance effect was obtained at about 180 cm^{-1} due to coupling between sharp A$_1$(TO$_1$ and TO$_2$) modes [44]. The appearance of a peak at 305 cm^{-1} in the ceramics indicates (at least at a local order) the asymmetry of octahedral [TiO$_6$] clusters within the BSZT tetragonal

Fig. 3 Schematic representation of crystalline supercells for BSZT ceramics with **a** $x = 0$, and **b** $x \approx 0.02$
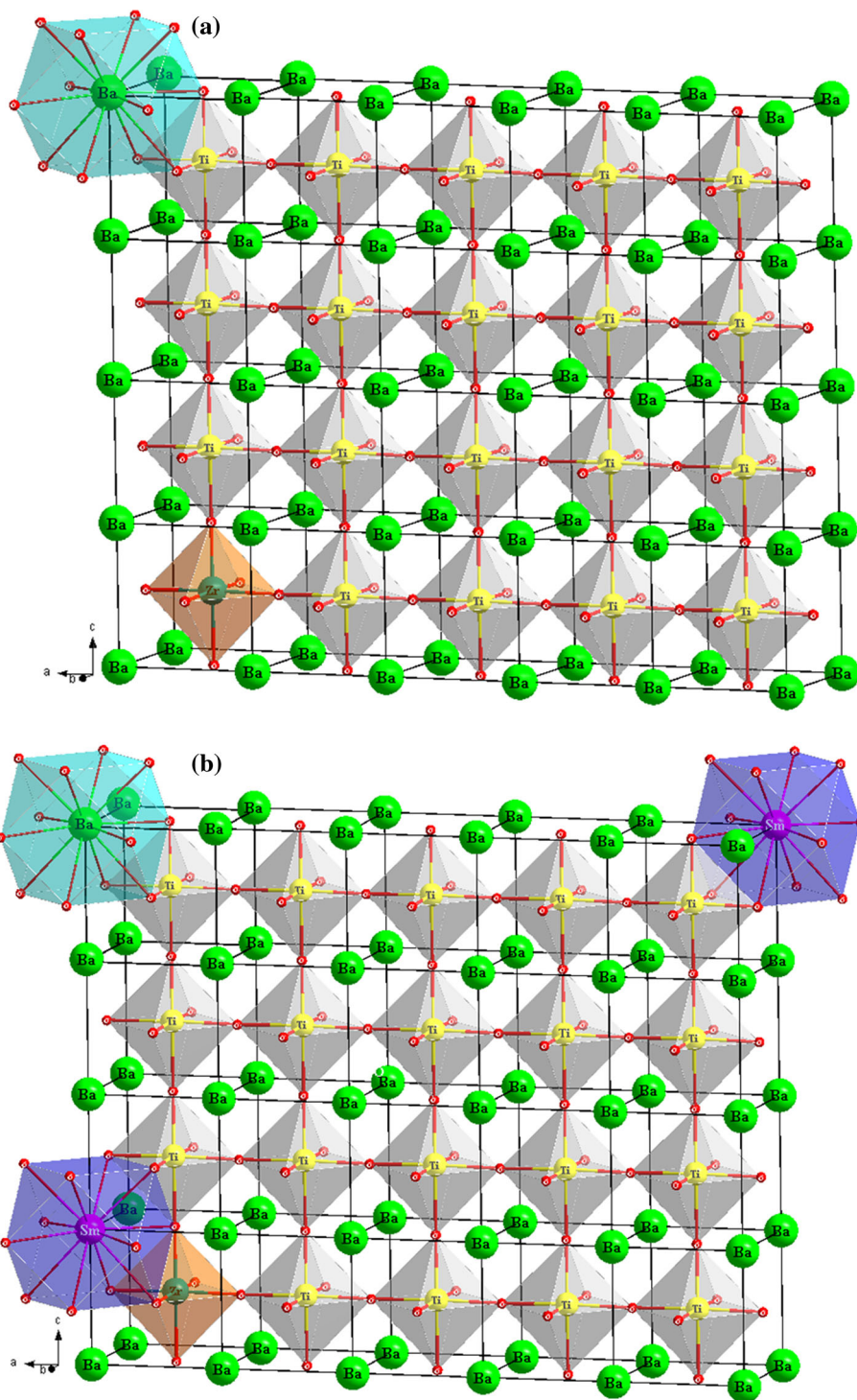

structure. A weak swelling at 453 cm^{-1} is attributed to overlapping E(TO$_3$) + E(LO$_2$) optical modes. A mode at 834 cm^{-1} is observed which mostly persists in a series of complex perovskites as a function of the perovskite unit cell and with changes in ionic radii. In this mode, neither A^{2+} or B^{4+} ions vibrate, but the mode still reflects changes in the perovskite structure; and the mode is due only to oxygen ion movement. The doping of different radii ions (Sm^{3+} in place of Ba^{2+}) at the A-site results in the formation of in equivalent oxygen octahedral that changes the spacing between A and B ions. Persistence of the mode at 721 cm^{-1} on doping and even after an increase in its content confirms short range polar ordering and lattice strain which are induced by rare earth [45].
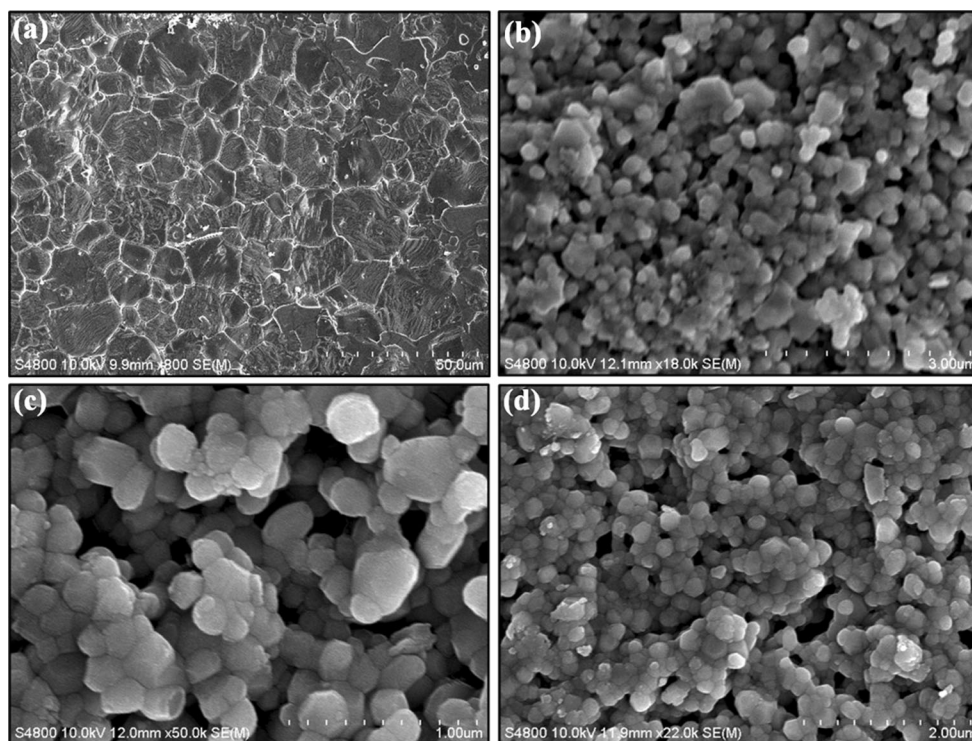
Fig. 4 SEM images of sintered BSZT pellet sintered at 1,200 °C for 4 h with different compositions **a** $x = 0$; **b** $x = 0.01$; **c** $x = 0.02$, and **d** $x = 0.03$
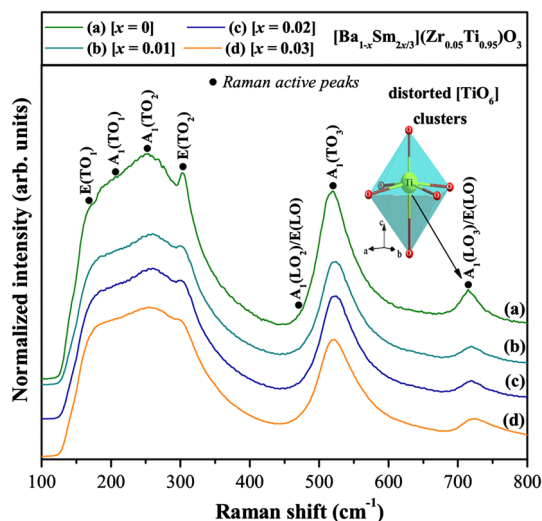

Fig. 5 M-Raman spectra of the $[Ba_{1-x}Sm_{2x/3}](Zr_{0.05}Ti_{0.95})O_3$ ceramics with [$x = 0$, 0.01, 0.02, and 0.03], respectively

3.6 Dielectric analyses

Dielectric properties of $[Ba_{1-x}Sm_{2x/3}](Zr_{0.05}Ti_{0.95})O_3$ ceramics with [$x = 0$, 0.01, 0.02, and 0.03] illustrated in Fig. 6a–d as a function of the temperature at different frequencies and comparison at 1 MHz for different compositions are shown in Fig. 6e.

In the raw pure BZT ceramic, three different phase transitions were observed. The first peak represents the cubic-to-tetragonal transition (the paraelectric-to-ferroelectric phase transition); i.e., for T_m or (T_c), the second peak represents a ferroelectric to another ferroelectric transition where the structure changes from tetragonal to orthorhombic, the third peak again represents a ferroelectric-to-ferroelectric transition, and the structure changes from orthorhombic to rhombohedral. With an increase in Sm^{3+} ion doping, all three peaks merge, and there is a decrease in the transition temperature as well as the dielectric constant. Similar type of decrease of transition temperature due to the rare earth incorporation in the BZT ceramics is reported [46, 47]. The lattice distortion and compositional fluctuation resulted in the parent doped BSZT ceramic due to the introduction of rare earth Sm^{3+} ions in the A-site which could be responsible for this kind of dielectric behavior.

According to Ostos et al. [25], the substitution of Ba^{2+} ions by Sm^{3+} ions in A-sites causes distortions in the BZT structure due to different atomic radii. Based on these hypotheses, we suppose that the substitution of Ba sites commonly occupied by Sm atoms causes an electronic compensation through the formation of barium vacancies (V''_{Ba}). In this case, it is very probable that the Sm atoms are coordinated to twelve oxygen (O) atoms (distorted cuboctahedral $[SmO_{12}]$ clusters); Ba atoms are bonded to twelve
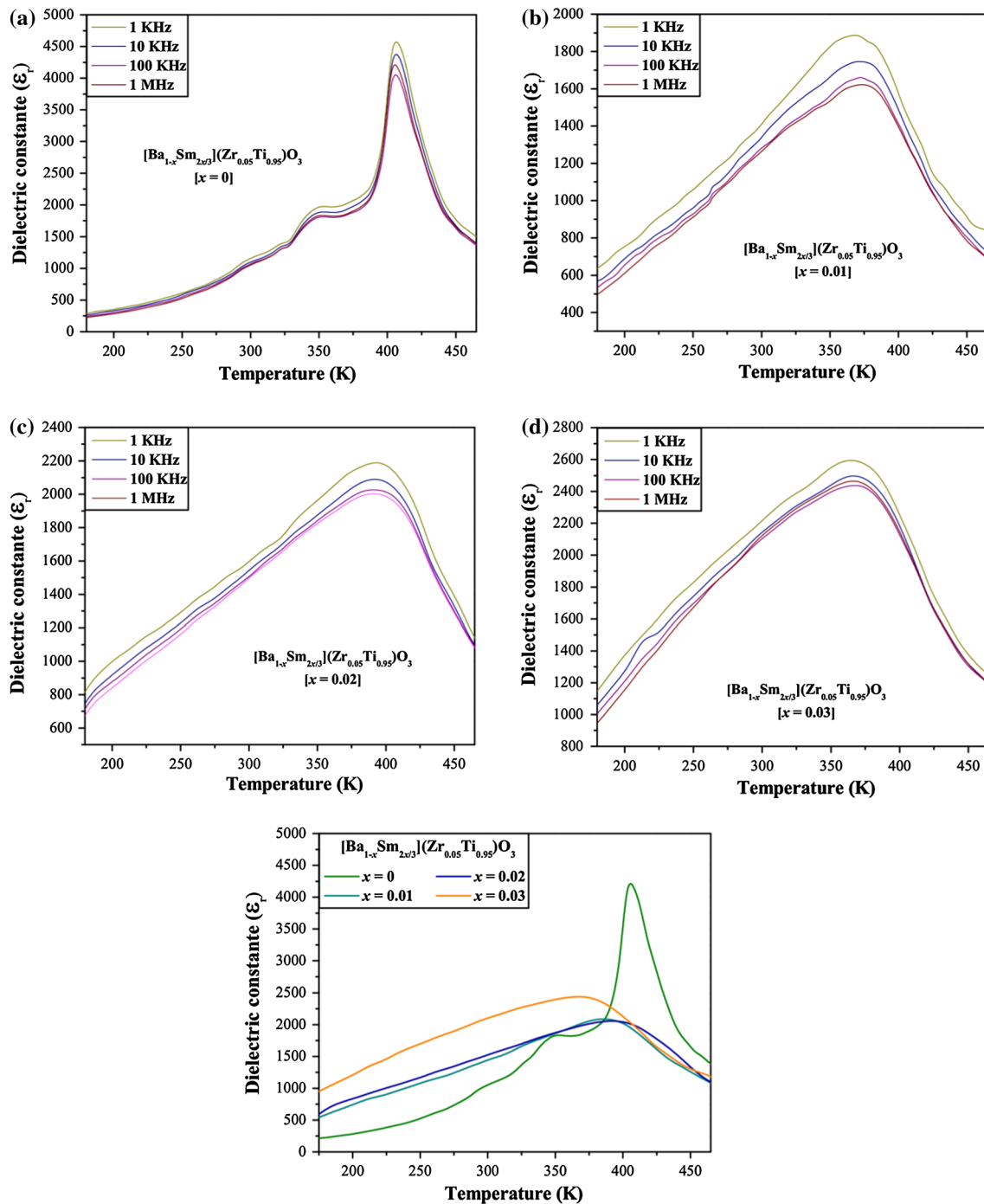
Fig. 6 Temperature dependent dielectric properties of $[Ba_{1-x}Sm_{2x/3}](Zr_{0.05}Ti_{0.95})O_3$ at different frequencies with different compositions **a** $x = 0$; **b** $x = 0.01$; **c** $x = 0.02$, and **d** $x = 0.03$ and comparison at 1 MHz with different compositions

oxygen atoms to forming the cuboctahedral configuration for $[BaO_{12}]$ clusters. However, substitution processes for cuboctahedral $[BaO_{12}]$ clusters by distorted cuboctahedral $[SmO_{12}]$ clusters can be obtained by the following Kröger-Vink notation described by Eq. (2) below:

$$Sm_2O_3 \rightarrow 2Sm_{Ba}^{\cdot} + V_{Ba}'' + 3O_O^x \qquad (2)$$
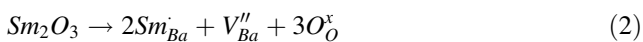
This equation implies that, for every two Sm^{3+} ions positioned on the A-site, one cationic vacancy V_{Ba}'' is necessary to promote the charge neutrality in the perovskite structure which produces compositional fluctuation on a microscopic scale. Replacing Ba^{2+} ions by Sm^{3+} ions results in A-site deficiency to maintain charge neutrality which increases

with a raise in the Sm^{3+} ions content. Again the change in the lattice parameter shrinkage causes the unit cell to off center Ti^{4+} ions out of the B-site, so that coupling between octahedral [TiO$_6$] clusters weakens and results in a strong decrease in the transition temperature.

The dielectric constant for all BSZT ceramics also shows a diffuse phase transition behavior (Fig. 7).

The diffuseness of a phase transition is described by the modified Curie–Weiss law as

$$\frac{1}{\varepsilon} - \frac{1}{\varepsilon_m} = \frac{(T - T_m)^{\gamma}}{C_1} \quad (T - T_m) \tag{3}$$

where γ and C_1 are assumed to be constants. The parameter, γ provides information on the character of the phase transition; for $\gamma = 1$, a normal Curie–Weiss law is obtained, for $\gamma = 2$, it reduces to the quadratic dependency which describes a complete diffuse phase transition. The plot of ln $(1/\varepsilon - 1/\varepsilon_m)$ vs ln $(T - T_m)$ at different frequencies is shown in Fig. 7, and a linear relationship is observed. The diffusivity increases with a raise in the Sm^{3+} ions content. The broadness or diffusiveness occurs mainly due to compositional fluctuation and structural disordering in the arrangement of cation in one or more crystallographic site of the structure. The incorporation of Sm^{3+} ions in the BZT lattice removes oxygen from the lattice which may produce a partial disconnection of the ferroelectric-active corner-shared octahedral [TiO$_6$] clusters [48]. As a result, a compositionally more disordered state appears, and the ferroelectric phase transition becomes smeared out by the chemical inhomogeneity.
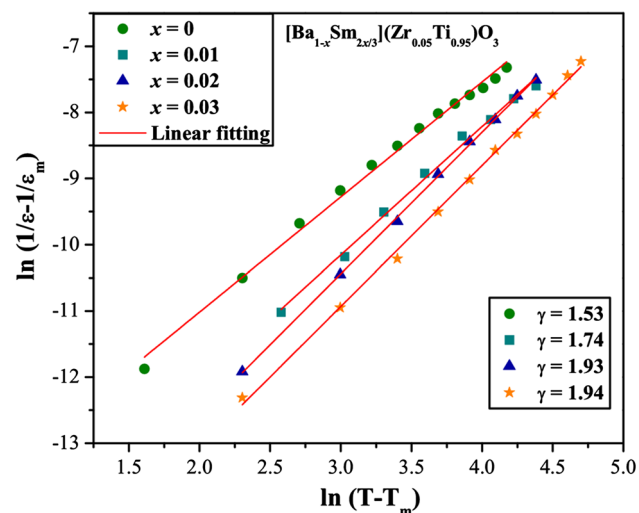
3.7 Ferroelectric analyses

The ferroelectric behavior of [Ba$_{1-x}$Sm$_{2x/3}$](Zr$_{0.05}$Ti$_{0.95}$)O$_3$ ceramics with [$x = 0$, 0.01, 0.02, and 0.03] was studied by a P–E hysteresis loop as shown in Fig. 8 using a maximum applied electric field of 10 kV/cm at room temperature.

A well saturated hysteresis loop was observed in all compositions with an increase in the remnant polarization and the coercive field. Ferroelectric properties are affected by composition, its homogeneity, defects, external field and orientation of domains which eventually contribute to the response of the material. Uniform oriented domain structures actually increase the ferroelectric properties. As observed from hysteresis curves, the remnant polarization increases monotonously as the Sm^{3+} ion content is increased. Note that Sm^{+3} ions substituents soften materials and results in an increase in squareness with an increase in the BZT lattice coercivity. According to "soft" and "hard" additive models, in soft ferroelectrics, cation vacancies generated by the donor Sm^{3+} ions doping ion cause domain motion and easier polarization switching which results in ferroelectric property enhancements. In our present study, squareness increases after Sm^{3+} ions substitution which is an important feature for their application in non-volatile random-access memory (NVRAM) without compromising ferroelectric properties and the coercive field. Finally, all the electrical parameters obtained for BSZT ceramics are presented in Table 2.

3.8 Piezoelectric analyses

Figure 9 shows the piezoelectric constant (d_{33}) variation as a function of [Ba$_{1-x}$Sm$_{2x/3}$](Zr$_{0.05}$Ti$_{0.95}$)O$_3$ ceramics with [$x = 0$, 0.01, 0.02, and 0.03].

Fig. 7 Plot of ln $(1/\varepsilon - 1/\varepsilon_m)$ as a function of ln $(T - T_m)$ of [Ba$_{1-x}$Sm$_{2x/3}$](Zr$_{0.05}$Ti$_{0.95}$)O$_3$ ceramics at frequency 1 MHz with different compositions **a** $x = 0$; **b** $x = 0.01$; **c** $x = 0.02$, and **d** $x = 0.03$

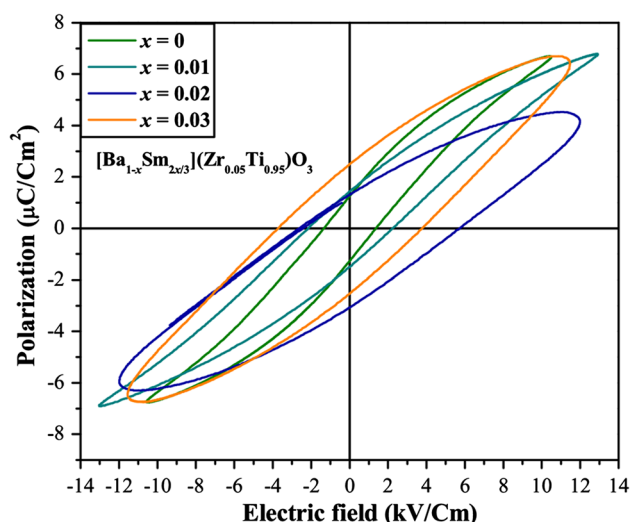Fig. 8 P–E hysteresis loop of [Ba$_{1-x}$Sm$_{2x/3}$](Zr$_{0.05}$Ti$_{0.95}$)O$_3$ ceramics with different compositions [$x = 0$, 0.01, 0.02, and 0.03]

Table 2 Parameters obtained from temperature dependent dielectric studies at 100 kHz on the composition of $[Ba_{1-x}Sm_{2x/3}](Zr_{0.05}Ti_{0.95})O_3$ ceramics with different Sm^{3+} ions content

$[Ba_{1-x}Sm_{2x/3}]$ $(Zr_{0.05}Ti_{0.95})O_3$ ceramics (x)	T_m (T–C) (K)	ε_m	P_r ($\mu C/cm^2$)	E_c (kV/cm)	γ
$x = 0$	406	4,200	1.3	1.17	1.53
$x = 0.01$	392	2,081	1.56	2.09	1.74
$x = 0.02$	385	2,137	1.99	2.69	1.93
$x = 0.03$	372	2,458	3.11	3.82	1.94

Piezoelectric properties in ferroelectric materials are due to electrostriction coupling with spontaneous polarization, P_s, expressed as [49]:

$$d_{33} = 2\varepsilon_{33}\varepsilon_0 k_{33}P_s \tag{4}$$

where ε_{33} is the dielectric constant, and ε_o is he dielectric constant of free space. Electrostrictive coupling originates from the anharmonic motion of dipoles in materials which causes a change in the lattice parameter and produces a strain. Substitution of the piezoelectric coefficients decreases with Sm^{3+} ions. Two major contributions to piezoelectric coefficients are extrinsic and intrinsic. The influence of grain size, preferred orientation and morphotropic phase boundary conditions determine the intrinsic component of the piezoelectric constant in a specimen [50, 51]. The extrinsic contribution is related to 180° and 90° domain wall motion in the specimen [52]. SEM images confirm that the grain size decreases with Sm^{3+} ion content. The decrease in the piezoelectric coefficient is attributed to the decrease in the grain size as the grain size
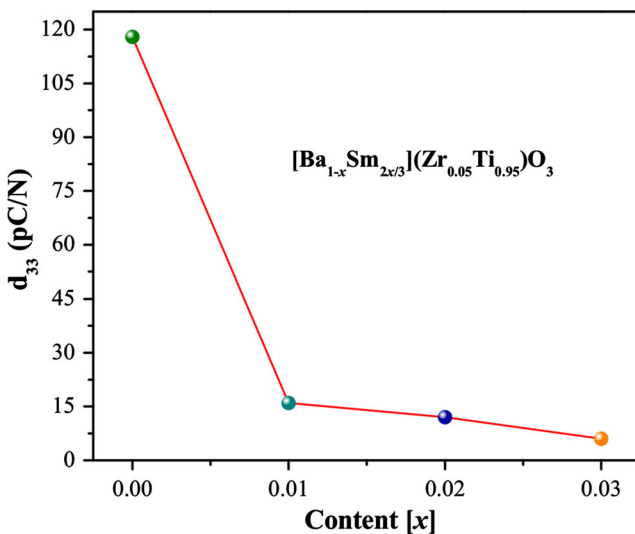
Fig. 9 Variation of piezoelectric constant (d_{33}) as a function of Sm^{3+} ions content

affects intrinsic responses and hence the domain wall motion [53].

3.9 UV–vis diffuse reflectance spectroscopy analyses

The optical band gap energy (E_{gap}) was calculated by the method proposed by Kubelka and Munk [54] which is based on the transformation of diffuse reflectance measurements to estimate E_{gap} values with good accuracy within the limits of assumptions when they are modeled in three dimensions [55]. In particular, it is useful in limited cases of an infinitely thick sample layer. The Kubelka–Munk equation for any wavelength is described by Eq. (5):

$$F(R_\infty) = \frac{(1 - R_\infty)^2}{2R_\infty} = \frac{k}{s} \tag{5}$$

where $F(R_\infty)$ is the Kubelka–Munk function or absolute reflectance of the sample. In our case, magnesium oxide (MgO) was the standard sample in reflectance measurements. $R_\infty = R_{sample}/R_{MgO}$ (R_∞ is the reflectance when the sample is infinitely thick), k is the molar absorption coefficient, and s is the scattering coefficient. In a parabolic band structure, the optical band gap and the absorption coefficient of semiconductor oxides [56] can be calculated by Eq. (6):

$$\alpha h\nu = C_1(h\nu - E_{gap})^n \tag{6}$$

where α is the linear absorption coefficient of the material, $h\nu$ is the photon energy, C_1 is a proportionality constant, E_{gap} is the optical band gap and n is a constant associated with different kinds of electronic transitions ($n = 1/2$ for a direct allowed, $n = 2$ for an indirect allowed, $n = 1.5$ for a direct forbidden and $n = 3$ for an indirect forbidden). According to the literature [57], titanate-zirconates exhibit an optical absorption spectrum governed by direct electronic transitions. In this phenomenon, after the electronic absorption process, electrons located in maximum energy states in the VB revert to minimum-energy states in the CB under the same point in the Brillouin zone [58]. Based on this information, E_{gap} values for BZT ceramic powder were calculated using $n = 2$ in Eq. 6. Finally, using the remission function described in Eq. 5 with $k = 2\alpha$, we obtain the modified Kubelka–Munk equation as indicated in Eq. (7):

$$[F(R_\infty)h\nu]^{1/2} = C_1(h\nu - E_{gap}) \tag{7}$$

Therefore, finding the $F(R_\infty)$ value from Eq. (7) and plotting a graph of $[F(R_\infty)h\nu]^{1/2}$ against $h\nu$, we can determine E_{gap} values for our $[Ba_{1-x}Sm_{2x/3}](Zr_{0.05}Ti_{0.95})O_3$ ceramics with [$x = 0$, 0.01, 0.02, and 0.03] with greater accuracy by extrapolating the linear portion of UV–vis curves.
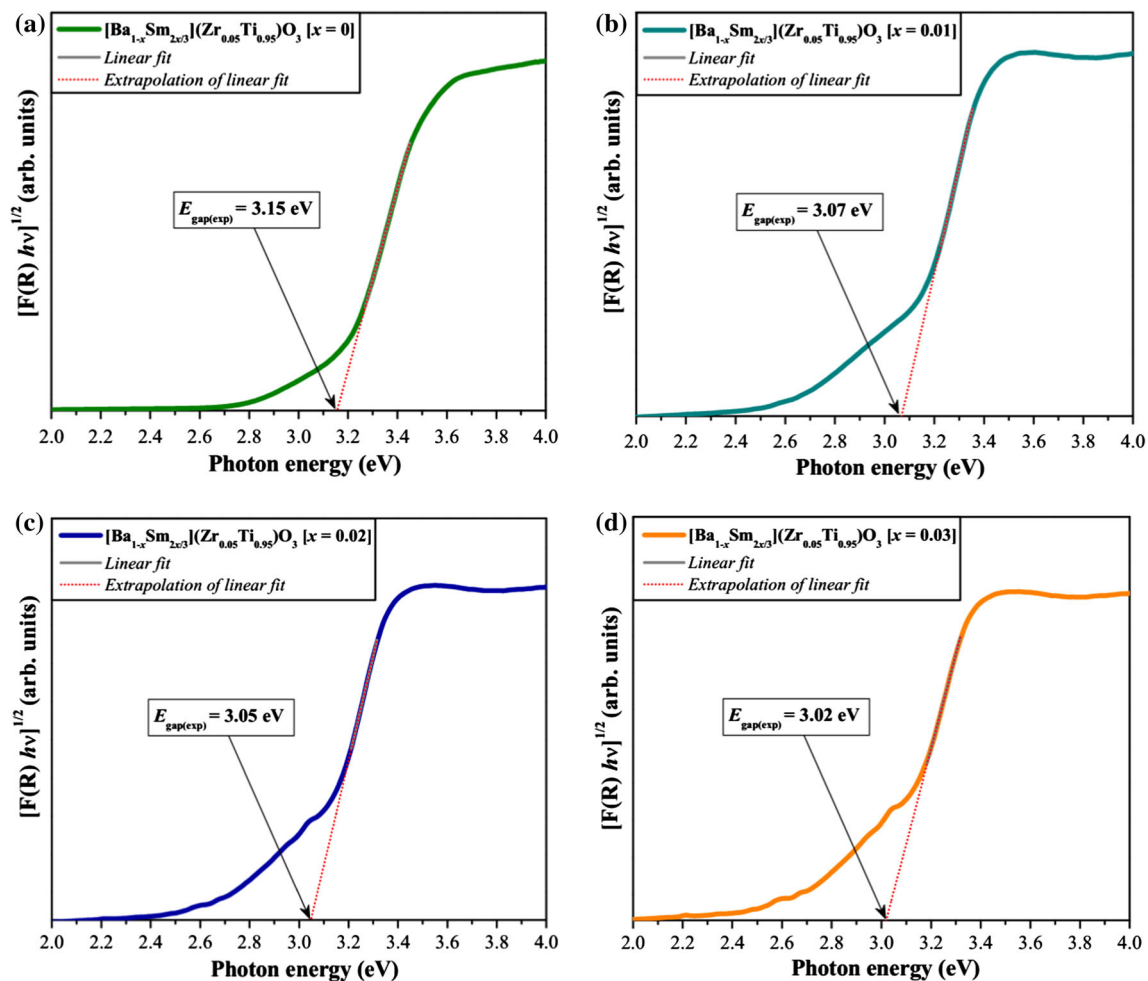
Fig. 10 UV-vis spectra of $[Ba_{1-x}Sm_{2x/3}](Zr_{0.05}Ti_{0.95})O_3$ powders with different compositions **a** $x = 0$; **b** $x = 0.01$; **c** $x = 0.02$, and **d** $x = 0.03$

Figure 10a–d show UV–vis spectra where we employed Eq. (7) by extrapolating the linear portion of UV–vis curves to calculate approximate E_{gap} values of $[Ba_{1-x}Sm_{2x/3}]$ $(Zr_{0.05}Ti_{0.95})O_3$ ceramics with [$x = 0, 0.01, 0.02$ and 0.03] heat treated at 1,100 °C for 4 h.

Distinct E_{gap} values calculated from UV–vis absorption spectra indicated the existence of intermediary energy levels within the optical band gap. These energy states are basically composed of O $2p$ orbitals (near the VB) as well as Ti $3d$ orbitals and Zr $4d$ orbitals (below the CB) [59]. The origin of these orbitals or energy levels is directly related to structural order–disorder in the random lattice which is a consequence of a symmetry break between O–Zr–O, O–Ti–O and/or O–Sm–O bonds (oxygen vacancies) and/or distortions on octahedral $[TiO_6]$ clusters [60]. Figure 10 also confirms that E_{gap} values decrease with an increase in Sm^{3+} ion content. Similar decrement in E_{gap} is also reported by authors in $BaTiO_3$ and BZT ceramics [61, 62]. Obtained E_{gap} values for doped ceramics can be associated with the structural disorder introduced in the lattice due to the creation of an A-site

vacancy and distortions in $[TiO_6]$ clusters. A-site vacancies increase with an increase in Sm content and result the formation of a larger number of shallow defects. Distortion in the octahedral $[TiO_6]$ increases with a raise in Sm content; thus the band gap decreases further [63].

4 Conclusions

In summary, $[Ba_{1-x}Sm_{2x/3}](Zr_{0.05}Ti_{0.95})O_3$ ceramics with [$x = 0.00, 0.01, 0.02$, and 0.03] were successfully prepared by high energy ball milling at 1,100 °C for 4 h. XRD patterns and M-Raman spectra revealed that all these ceramics have a single phase with a perovskite-type tetragonal structure and a space group of $P4/mmm$. Rietveld refinement data were employed to model $[BaO_{12}]$, $[SmO_{12}]$ $[ZrO_6]$, and $[TiO_6]$ clusters by means of lattice parameters and atomic positions. SEM images confirm that the grain size decreases with an increase in Sm^{3+} ions content. The dielectric study of all compositions shows a normal ferroelectric character with a

decrease in the Curie temperature and an increase in Sm^{3+} ions content. The phase transition diffusivity increases with a variation in Sm^{3+} ions content. P–E hysteresis loops showed an increment in the remnant polarization and the coercive field with Sm^{3+} ions content. The piezoelectric coefficient decreases with Sm^{3+} ions doping. The optical band gap of the ceramics was obtained from UV–vis spectroscopy which revealed a decrease with the increase of Sm^{3+} ions content due to the formation of oxygen vacancies and the induction of lattice distortions.

References

1. Z. Yu, C. Ang, R. Guo, A.S. Bhalla, Piezoelectric and strain properties of $Ba(Ti_{1-x}Zr_x)O_3$ ceramics. J. Appl. Phys. **92**, 1489–1493 (2002)

2. T.B. Wu, C.M. Wu, M.L. Chen, Highly insulative barium zirconate-titanate thin films prepared by rf magnetron sputtering for dynamic random access memory applications. Appl. Phys. Lett. **69**, 2659 (1996)

3. X.G. Tang, J. Wang, X.X. Wang, H.L.W. Chan, Effects of grain size on the dielectric properties and tunabilities of sol–gel derived Ba(Zr0.2Ti0.8)O3 ceramics, Sol. State Commun. **131**, 163–168 (2004)

4. H. Tian, C. Hu, Q. Chen, Z. Zhou, High, purely electrostrictive effect in cubic $K_{0.95}Na_{0.05}Ta_{1-x}Nb_xO_3$ lead-free single crystals. Mater. Lett. **68**, 14–16 (2012)

5. B. Wang, C. Yang, H. Chen, J. Zhang, A. Yu, R. Zhang, Effects of oxygen to argon ratio on $Ba(Zr_{0.2}Ti_{0.8})O_3$ thin films prepared by RF magnetron sputtering. J. Mater. Sci. Mater. Elect, **20**(7), 614–618 (2009)

6. M.L.V. Mahesh, V.V. Bhanu Prasad, A.R. James, Effect of sintering temperature on the microstructure and electrical properties of zirconium doped barium titanate ceramics. J Mater. Sci. Mater. Elect. **24**(12), 4684–4692 (2013)

7. P.A. Jha, A.K. Jha, Effect of sintering temperature on the grain growth and electrical properties of barium zirconate titanate ferroelectric ceramics. J. Mater. Sci. Mater. Electr. **25**(5), 2305–2310 (2014)

8. S. Sen, R.N.P. Choudhary, Structural, dielectric and electrical properties of Ca modified $BaSn_{0.15}Ti_{0.85}O_3$ ceramics. J. Mater. Sci. **40**, 5457–5462 (2005)

9. N. Ding, X.G. Tang, X.D. Ding, Q.X. Liu, Y.P. Jiang, L.L. Jiang, Effect of Zr/Ti ratio on the dielectric and piezoelectric properties of Mn-doped $Ba(Zr,Ti)O_3$ ceramics. J. Mater. Sci. Mater. Electr. **25**(5), 2305–2310 (2014)

10. L. Cao, W. Wang, G. Su, W. Liu, Synthesis, microstructure and dielectric properties of zirconium doped barium strontium titanate obtained by solvothermal method. J. Mater. Sci. Mater. Electr. **24**(7), 2234–2239 (2013)

11. Y. Wang, L. Li, J. Qi, Z. Gui, Ferroelectric characteristics of ytterbium-doped barium zirconium titanate ceramics. Ceram. Int. **28**, 657–661 (2002)

12. W. Li, Z. Xu, R. Chu, P. Fu, P. An, Effect of Ho doping on piezoelectric properties of BCZT ceramics. Ceram. Inter. **38**, 4353–4355 (2012)

13. D. Shan, Y.F. Qu, J.J. Song, Dielectric properties and substitution preference of yttrium doped barium zirconium titanate ceramics. Solid State Commun. **141**, 65–68 (2007)

14. S. Bhaskar-Reddy, M.S. Ramachandra-Rao, K. Prasad-Rao, Observation of high permittivity in Ho substituted $BaZr_{0.1}Ti_{0.9}O_3$ ceramics. Appl. Phys. Lett. **91**, 022917–022919 (2007)

15. X. Chou, J. Zhai, H. Jiang, X. Yao, Dielectric properties and relaxor behavior of rare-earth (La, Sm, Eu, Dy, Y) substituted barium zirconium titanate ceramics. J. Appl. Phys. **102**, 084106–084111 (2007)

16. K. Aliouane, A. Guehria-Laidoudi, A. Simon, J. Ravez, Study of new relaxor materials in $BaTiO_3$–$BaZrO_3$–$La_{2/3}TiO_3$ system. Solid State Sci. **7**, 1324–1332 (2005)

17. F. Moura, A.Z. Simões, L.S. Cavalcante, M. Zampieri, J.A. Varela, E. Longo, M.A. Zaghete, M.L. Simões, Strain and vacancy cluster behavior of vanadium and tungsten-doped $Ba[Zr_{0.10}Ti_{0.90}]O_3$ ceramics. Appl. Phys. Lett. **92**, 032905–032907 (2008)

18. H. Kishi, N. Kohzu, J. Sugino, H. Ohsato, Y. Iguchi, T. Okuda, The effect of rare-earth (La, Sm, Dy, Ho and Er) and Mg on the microstructure in $BaTiO_3$. J. Eur. Ceram. Soc. **19**, 1043–1046 (1999)

19. S. Shirasaki, Origin of semiconductng behavior in rare-earth-doped barium titanate. Solid State Commun. **19**(721), 721–724 (1976)

20. N.V. Dergunova, E.G. Fesenko, V.P. Sakhnenko, Rendering barium titanate semiconductive by doping with rare earth elements. Ferroelectrics **83**, 187–191 (1988)

21. K. Watanabe, H. Ohsato, H. Kishi Y Okino, N. Kohzu, Y. Lguchi, T. Okuda, Solubility of La–Mg and La–Al in $BaTiO_3$. *Solid State Ionics* **108**, 129–135 (1998)

22. J. Zhu, W.J. Jie, X.H. Wei, W.F. Qin, Y. Zhang, Y.R. Li, Enhanced dielectric characteristics of manganese-doped BZT thin films. Surf. Rev. Lett. **15**, 29–33 (2008)

23. R. Sagar, P. Hudge, S. Madolappa, A.C. Kumbharkhane, R.L. Raibagkar, Electrical properties and microwave dielectric behavior of holmium substituted barium zirconium titanate ceramics. J. Alloys Compd. **537**, 197–202 (2012)

24. F. Moura, A.Z. Simões, L.S. Cavalcante, M.A. Zaghete, J.A. Varela, E. Longo, Ferroelectric and dielectric properties of vanadium-doped $Ba(Ti_{0.90}Zr_{0.10})O_3$ ceramics. J Alloys Compd. **466**, L15–L18 (2008)

25. C. Ostos, L. Mestres, M.L. Martinez-Sarrión, J.E. Garcia, A. Albareda, R. Perez, Synthesis and characterization of A-site deficient rare-earth doped $BaZr_xTi_{1-x}O_3$ perovskite-type compounds. Solid State Sci. **11**, 1016–1022 (2009)

26. W. Cai, C. Fu, J.J. Gao, Effect of Mn doping on the dielectric properties of $BaZr_{0.2}Ti_{0.8}O_3$ ceramics. J Mater. Sci. Mater. Electron. **21**, 317–325 (2010)

27. S. Mahajan, O.P. Thakur, D.K. Bhattacharya, K. Sreenivas, Ferroelectric relaxor behaviour and impedance spectroscopy of Bi_2O_3-doped barium zirconium titanate ceramics. J. Phys. D Appl. Phys. **42**, 065413–065422 (2009)

28. S. Mahajan, O.P. Thakur, K. Sreenivas, C. Prakash, Effect of Nd doping on structural, dielectric and ferroelectric properties of $Ba(Zr_{0.05}Ti_{0.95})O_3$ ceramic, *Int*. Ferroelectrics **122**, 83–89 (2010)

29. S. Mahajan, O.P. Thakur, D.K. Bhattacharya, K. Sreenivas, S. Mahajan, O.P. Thakur, D.K. Bhattacharya, K. Sreenivas, A comparative study of $Ba_{0.95}Ca_{0.05}Zr_{0.25}Ti_{0.75}O_3$ relaxor ceramics prepared by conventional and microwave sintering techniques. Mater. Chem. Phys. **112**, 858–862 (2008)

30. J. Joseph, T.M. Vimala, J. Raju, V.R.K. Murthy, Structural investigations on the $(Ba,Sr)(Zr,Ti)O_3$ system. J. Phys. D Appl. Phys. **32**, 1049–1057 (1999)

31. A.K. Kalyani, A. Senyshyn, R. Ranjan, Polymorphic phase boundaries and enhanced piezoelectric response in extended

composition range in the lead free ferroelectric $BaTi_{1-x}Zr_xO_3$. J. Appl. Phys. **114**, 014102 (2013)

32. http://en.wikipedia.org/wiki/Octahedron

33. C. Duan, J. Yuan, J. Zhao, Luminescence properties of efficient X-ray phosphors of $YBa_3B_9O_{18}$, $LuBa_3(BO_3)_3$, α-$YBa_3(BO_3)_3$ and $LuBO_3$. J. Solid State Chem. **178**, 3698–3702 (2005)

34. http://en.wikipedia.org/wiki/Cuboctahedron

35. S. Shirasaki, H. Yamamura, H. Haneda, K. Kakegawa, J. Moori, Defect structure and oxygen diffusion in undoped and La doped polycrystalline barium titanate. J. Chem. Phys. **73**, 4640–4645 (1980)

36. A.F. Shimanskij, M. Drofenik, D. Kolar, Subsolidus grain growth in donor doped barium titanate. J. Mater. Sci. **29**, 6301–6305 (1994)

37. W. Yang, Y. Pu, X. Chen, J. Wang, Study of reoxidation in heavily La-doped barium titanate ceramics. J. Phys. Conf. Series. **152**, 012040–012045 (2009)

38. M.N. Rahaman, Ceramic processing and sintering, 2nd edn. (CRC Press, New York, 2005)

39. S.J.L. Kang, Sintering densification, grain growth, and microstructure, 1st edn. (Elsevier, Oxford, 2005)

40. T. Nakamura, T. Sakudo, Y. Ishibashi, Y. Tominaga, *Ferroelectricity involved in structural phase transition*, 1st edn. (Syokabo, Japan, 1988)

41. M.D. Domenico Jr, S.H. Wemple, S.P.S. Porto, P.R. Buman, Raman spectrum of single-domain $BaTiO_3$. Phys. Rev. **174**, 522–530 (1968)

42. A. Chaves, R.S. Katiyar, S.P.S. Porto, Coupled modes with A1 symmetry in tetragonal $BaTiO_3$. Phys. Rev. B. **10**, 3522–3533 (1974)

43. P.S. Dobal, A. Dixit, R.S. Katiyar, Effect of lanthanum substitution on the Raman spectra of barium titanate thin films. J. Raman Spectrosc. **38**, 142–146 (2007)

44. Y. Liu, Y. Feng, X. Wu, X. Han, Microwave absorption properties of La doped barium titanate in X-band. J. Alloys Compd. **472**, 441–445 (2009)

45. D. Shan, Y.F. Qu, J.J. Song, Dielectric properties and substitution preference of yttrium doped barium zirconium titanate ceramics. Solid State Commun. **141**, 65–68 (2007)

46. W. Cai, C. Fu, J. Gao, Z. Lin, X. Deng, Effect of hafnium on the microstructure, dielectric and ferroelectric properties of $Ba[Zr_{0.2}Ti_{0.8}]O_3$ ceramics. Ceram. Int. **38**, 3367–3375 (2012)

47. X. Diez-Betriu, J.E. Garcia, C. Ostos, A.U. Boya, D.A. Ochoa, L. Mestres, R. Perez, Phase transition characteristics and dielectric properties of rare-earth (La, Pr, Nd, Gd) doped $Ba(Zr_{0.09}Ti_{0.91})O_3$ ceramics. Mater. Chem. Phys. **125**, 493–499 (2011)

48. F.D. Morrison, D.C. Sinclair, A.R. West, Doping mechanisms and electrical properties of La-doped $BaTiO_3$ ceramics. Int. J. Inorg. Mater. **3**, 1205–1210 (2001)

49. A.V. Bune, C. Zhu, S. Ducharme, L.M. Blinov, V.M. Fridkin, Piezoelectric and pyroelectric properties of ferroelectric Langmuir–Blodgett polymer films, J. Appl. Phys. **85**, 7869–7873 (1999)

50. S. Tsurekawa, K. Ibaraki, K. Kawahara, T. Watanabe, The continuity of ferroelectric domains at grain boundaries in lead zirconate titanate. Scrip. Mater. **56**, 577–580 (2007)

51. Y. Chang, Z. Yang, L. Wei, Microstructure, density, and dielectric properties of lead-free $(K_{0.44}Na_{0.52}Li_{0.04})(Nb_{0.96-x}Ta_xSb_{0.04})O_3$ piezoelectric ceramics. J. Am. Ceram. Soc. **90**, 1656–1658 (2007)

52. K. Ramam, M. Lopez, Microstructure, dielectric and electromechanical properties of PLSZFT nanoceramics for piezoelectric applications. J. Mater. Sci.: Mater. Electron. **19**, 1140–1145 (2008)

53. P.A. Jha, A.K. Jha, Effects of yttrium substitution on structural and electrical properties of barium zirconate titanate ferroelectric ceramics. Curr. Appl. Phys. **13**, 1413–1419 (2013)

54. P. Kubelka, F. Munk-Aussig, Ein Beitrag zur Optik der Farban striche. Zeit. Für. Tech. Physik. **12**, 593–601 (1931)

55. A.E. Morales, E.S. Mora, Use of diffuse reflectance spectroscopy for optical characterization of un-supported nanostructures. U. Pal, Rev. Mex. Fis. S. **53**, 18–22 (2007)

56. R.A. Smith, *Semiconductors*, 2nd edn. (Cambridge University Press, London, 1978)

57. L.S. Cavalcante, N.C. Batista, T. Badapanda, M.G.S. Costa, M.S. Li, W. Avansi, V.R. Mastelaro, E. Longo, J.W.M. Espinosa, M.F.C. Gurgel, Local electronic structure, optical bandgap and photoluminescence (PL) properties of $Ba(Zr_{0.75}Ti_{0.25})O_3$ powders. Mater. Sci. Semicond. Process. **16**, 1035–1045 (2013)

58. L.S. Cavalcante, M.F.C. Gurgel, E.C. Paris, A.Z. Simões, M.R. Joya, J.A. Varela, P.S. Pizani, E. Longo, Combined experimental and theoretical investigations of the photoluminescent behavior of $Ba(Ti, Zr)O_3$ thin films. Acta Mater. **55**, 6416–6426 (2007)

59. M. Anicete-Santos, L.S. Cavalcante, E. Orhan, E.C. Paris, L.G.P. Simões, M.R. Joya, I.L.V. Rosa, P.R. de Lucena, M.R.M.C. Santos, L.S. Santos-Júnior, P.S. Pizani, E. R. Leite, J.A. Varela, E. Longo, The role of structural order–disorder for visible intense photoluminescence in the $BaZr_{0.5}Ti_{0.5}O_3$ thin films. Chem. Phys. **316**, 260–266 (2005)

60. C. Laulhé, F. Hippert, R. Bellissent, A. Simon, G.J. Cuello, Local structure in $BaTi_{1-x}Zr_xO_3$ relaxors from neutron pair distribution function analysis. Phys. Rev. B. **79**, 064104–064113 (2009)

61. S.K. Ghosh, M. Ganguly, S.K. Rout, S. Chanda, T.P. Sinha, Structural, optical and dielectric relaxor properties of neodymium doped cubic perovskite $Ba_{1-x}Nd_{2x/3})(Zr_{0.3}Ti_{0.7})O_3$. Solid State Sci. **30**, 68–77 (2014)

62. S.K. Rout, W.S. Woo, C.W. Ahn, I.W. Kim, Characterization of A-site deficient samarium doped barium titanate. Phys. B **411**, 26–34 (2013)

63. M.L. Moreira, M.F.C. Gurgel, G.P. Mambrini, E.R. Leite, P.S. Pizani, J.A. Varela, E. Longo, Photoluminescence of barium titanate and barium zirconate in multilayer disordered thin films at room temperature. J. Phys. Chem. A **112**, 8938–8942 (2008)